PNAS RESEARCH ARTICLE | APPLIED PHYSICAL SCIENCES

Structural phase purification of bulk HfO_2:Y through pressure cycling

J. L. Musfeldt[a,b,1], Sobhit Singh[c,d,1], Shiyu Fan[e], Yanhong Gu[a], Xianghan Xu[f,g], S.-W. Cheong[f,g], Z. Liu[h], David Vanderbilt[f], and Karin M. Rabe[f,1]

Contributed by Karin M. Rabe; received July 26, 2023; accepted December 5, 2023; reviewed by Beatriz Noheda and John S. Tse

We combine synchrotron-based infrared absorption and Raman scattering spectroscopies with diamond anvil cell techniques and first-principles calculations to explore the properties of hafnia under compression. We find that pressure drives HfO_2:7%Y from the mixed monoclinic ($P2_1/c$) + antipolar orthorhombic (*Pbca*) phase to pure antipolar orthorhombic (*Pbca*) phase at approximately 6.3 GPa. This transformation is irreversible, meaning that upon release, the material is kinetically trapped in the *Pbca* metastable state at 300 K. Compression also drives polar orthorhombic ($Pca2_1$) hafnia into the tetragonal ($P4_2/nmc$) phase, although the latter is not metastable upon release. These results are unified by an analysis of the energy landscape. The fact that pressure allows us to stabilize targeted metastable structures with less Y stabilizer is important to preserving the flat phonon band physics of pure HfO_2.

hafnia | phase purification | pressure cycling | competing phases | vibrational spectroscopies

Significance

In the last decade, the functional possibilities of metastable phases of HfO_2, including the orthorhombic ferroelectric phase and the antipolar *Pbca* phase, have stimulated intense experimental and theoretical research effort. Synthesis of several of these phases as bulk single crystals has been achieved with ultra-high-temperatures and rapid quenching in combination with Y stabilizer concentrations of up to 20%. Here, we show how to access the antipolar phase and a theoretically predicted metastable tetragonal phase at room temperature using pressure cycling with reduced Y concentration, yielding samples closer to the ideal of pure HfO_2.

The simple binary composition of hafnia (HfO_2) belies a complex energy landscape with many competing phases (1). In addition to the monoclinic $P2_1/c$ bulk ground state, other reported metastable phases include an antipolar orthorhombic *Pbca* phase and a polar orthorhombic $Pca2_1$ phase. This presents both challenges and opportunities in realizing the properties of these materials for applications (2–8) and identifying pathways by which these phases can be reached is of great interest (9–12). In particular, the observation of ferroelectricity in thin films (13–16) and the prediction of flat bands and scalable ferroelectricity in the metastable polar orthorhombic phase of hafnia is generating high hopes for the prospect of single atom memory (17). Achieving the dream of atomically sharp domains acting as individually switchable dipoles (17) requires meeting the synthetic challenge for high-quality polar orthorhombic HfO_2 as a physical platform for such a device (1, 18).

Efforts to grow single crystals of ferroelectric HfO_2 have relied on high-temperature laser floating zone techniques, rapid temperature quenching, and use of Y as a stabilizer (19–22). Pressure represents another tool to navigate the complex energy landscapes and access metastable phases, with the best-known example being the development of synthetic diamond. Previous pressure studies of hafnia have focused on the phase sequence starting with the ambient monoclinic phase (23–32). Whether metastable phases of interest—particularly the ferroelectric and antipolar phases—can be accessed and potentially stabilized with pressure rather than temperature and then recovered to ambient conditions is currently underexplored. This type of analysis of phase stability is also relevant to thin films, although there, strain is a better control parameter.

In this work, we investigate pressure-induced phases and reversibility on release of pressure in HfO_2:x%Y ($x = 0, 7, 11, 12, 20$), which under ambient conditions hosts, respectively, a monoclinic phase ($P2_1/c$), a mixed phase ($P2_1/c$ + *Pbca*), an antipolar orthorhombic (*Pbca*) phase, a polar orthorhombic ($Pca2_1$) phase, and a cubic ($Fm\bar{3}m$) phase (Fig. 1 and *SI Appendix*, Table S1) (20, 33). Previous efforts reveal that these phases can be identified by their vibrational fingerprints via a combination of synchrotron-based infrared absorption and Raman scattering combined with complementary lattice dynamics calculations (34, 35). This approach is successful because the irreducible representations of distinct crystal phases exhibit the full crystal symmetry. Here, we show that this approach can be extended to elevated pressures using diamond anvil cell techniques to identify different forms of the material under pressure cycling up to 27 GPa. For the majority of doping concentrations, our room temperature measurements show reversible pressure-induced structural changes which are in excellent agreement with predictions from our first-principles calculations. For instance, there is a reversible transition from the polar orthorhombic to the tetragonal phase at Y stabilizer concentrations that are significantly lower than what might be expected.

Author contributions: J.L.M. and S.S. designed research; J.L.M., S.S., S.F., Y.G., X.X., S.-W.C., Z.L., D.V., and K.M.R. performed research; J.L.M., S.S., X.X., S.-W.C., D.V., and K.M.R. analyzed data; and J.L.M. and S.S. wrote the paper.

Reviewers: B.N., Zernike Institute for Advanced Materials, University of Groningen; and J.S.T., University of Saskatchewan.

The authors declare no competing interest.

[1]To whom correspondence may be addressed. Email: musfeldt@utk.edu, s.singh@rochester.edu, or kmrabe@physics.rutgers.edu.

This article contains supporting information online at https://www.pnas.org/lookup/suppl/doi:10.1073/pnas.2312571121/-/DCSupplemental.

Published January 24, 2024.

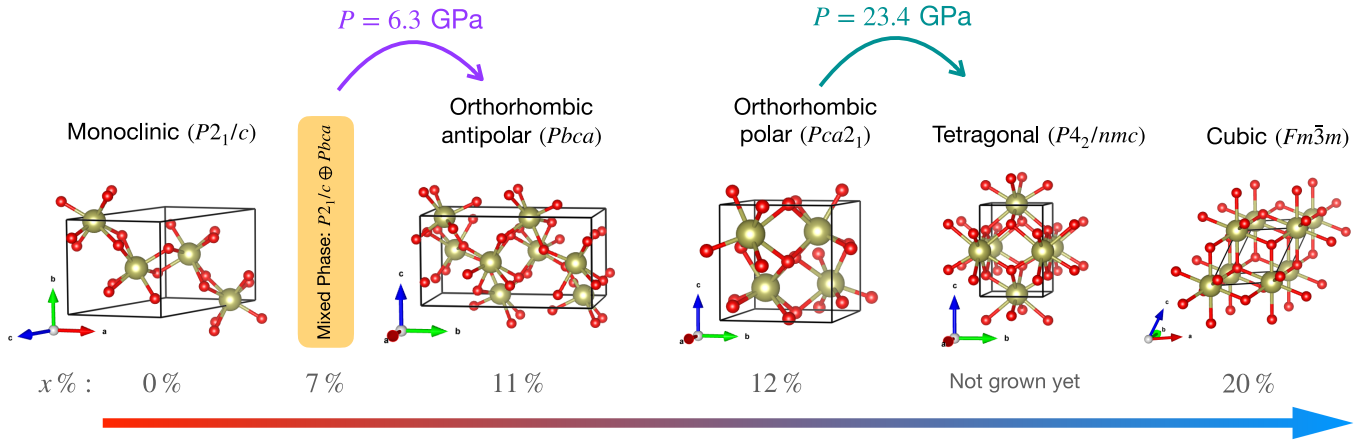

Fig. 1. Summary of the various phases of hafnia of interest in this work, i.e., monoclinic HfO_2 (the ground state), and the higher-energy metastable phases arranged in the order of their increasing formation energy. When formed by laser floating zone + rapid cooling techniques (20), Y concentrations of 0, 7, 11, 12, and 20% yield monoclinic, mixed monoclinic and antipolar orthorhombic, antipolar orthorhombic, polar orthorhombic, and cubic phases, respectively. A metastable tetragonal phase has been predicted from first principles but not yet realized by these growth methods. X-ray scattering as well as TEM studies of the initial products of this study are available in ref. 20. The space groups are indicated above. The polar orthorhombic material is switchable (i.e., ferroelectric), whereas antipolar orthorhombic hafnia is not switchable (i.e., not antiferroelectric) (20). The curved arrows at the top indicate the pressure-induced transitions discussed in the text.

Moreover, for $x = 7\%$, we find that a mixed monoclinic + antipolar phase sample is converted to a pure antipolar phase at approximately 6.3 GPa. Remarkably, this transition is irreversible upon release, demonstrating that pressure cycling provides a route to clean, phase-pure materials. This work opens the door to the design of more complex protocols involving pressure cycling in conjunction with chemical stabilization that may ultimately provide a route to kinetic trapping of the sought-after ferroelectric orthorhombic phase of hafnia.

Results and Discussion

Pressure-Induced Mixed-to-Antipolar-Orthorhombic Transition in HfO_2:7%Y. Fig. 2*A* displays the Raman scattering response of HfO_2:7%Y at ambient conditions. According to our X-ray analysis, this system hosts a mixed monoclinic ($P2_1/c$) + antipolar orthorhombic ($Pbca$) structure (*SI Appendix*, Fig. S2). The Raman spectrum therefore contains phonons from both phases—a finding that we confirm by a comparison with complementary lattice dynamics calculations (Fig. 2*A*) (34). Most of the time, we would consider this to be an extremely low-quality "dirty" sample. As we show below, it turns out to be an excellent precursor to "clean" pure-phase materials.

Fig. 2*B* shows the Raman scattering response of HfO_2:7%Y under pressure. There is a clear structural phase transition from mixed phase (monoclinic + antipolar orthorhombic) to pure antipolar orthorhombic ($Pbca$) structure at 6.3 GPa. This is interesting because it normally requires 11% Y stabilizer to trap the antipolar orthorhombic phase when prepared by laser floating zone + rapid cooling techniques (20). Strikingly, the mixed phase to pure antipolar orthorhombic transition is irreversible upon release of the pressure (Fig. 2*C*). In other words, a 6.3-GPa pressure cycle traps pure antipolar orthorhombic hafnia in a metastable state with only 7% Y doping—a reduction of 36%. The infrared response under pressure is consistent with these findings. We discuss the dirty to clean transition in terms of overall phase stability below.

We also investigated the stability of this pressure-cycled material. Specifically, we sought to test whether antipolar orthorhombic HfO_2:7%Y is transient (reverting to a mixed ground state over time) or a pure long-lived metastable state akin to diamond. Raman scattering spectroscopy reveals that antipolar orthorhombic HfO_2:7%Y prepared in this manner is stable immediately after release, at the 5 d mark, and over more than four months. We therefore conclude that antipolar orthorhombic HfO_2:7%Y is metastable indefinitely at room temperature. To further explore the stability of this material, we heated the sample to 200 °C in a vacuum oven and remeasured the Raman response. There are no new peaks in the Raman scattering spectrum, so we conclude that any barrier to reversal is much larger than $k_BT = 200$ °C. These data are shown in *SI Appendix*.

Antipolar Orthorhombic HfO_2:7%Y at Higher Pressures. Having established the mixed phase to pure antipolar orthorhombic transition in HfO_2:7%Y at 6.3 GPa, we decided to continue compressing the sample to test whether the polar orthorhombic phase can be stabilized as well. While Raman scattering is the perfect technique to follow the mixed to antipolar transition as discussed above, we find that it is less useful at higher pressures because the sample starts to fluoresce—at least with a green laser. As a result, it is difficult to follow the phonons above approximately 20 GPa. We therefore turned to synchrotron-based far infrared spectroscopy to avoid the fluorescence and continue our search for evidence of the polar orthorhombic phase at pressures above 6.3 GPa.

Fig. 3 summarizes the synchrotron-based far-infrared response of HfO_2:7%Y as a function of pressure at 300 K. There are several noticeable changes above 20 GPa including i) strengthening of the low-frequency structure near 100 cm^{-1}, ii) formation of a weak feature near 225 cm^{-1}, iii) red shifting of the edge near 380 cm^{-1}, and iv) loss of structure near 540 cm^{-1}. Despite these signatures, the spectral response of this material is not compatible with expectations for pure-phase polar orthorhombic hafnia (34). Instead, it corresponds to the antipolar orthorhombic phase (34). The system remains in the antipolar orthorhombic phase upon release—not the mixed state—identical to what we described above. We therefore see that compression of HfO_2:7%Y provides a facile and reliable route to the antipolar orthorhombic phase. While this phase cannot be used for FeRAM devices, antiferroelectrics (switchable antipolar materials) are extremely

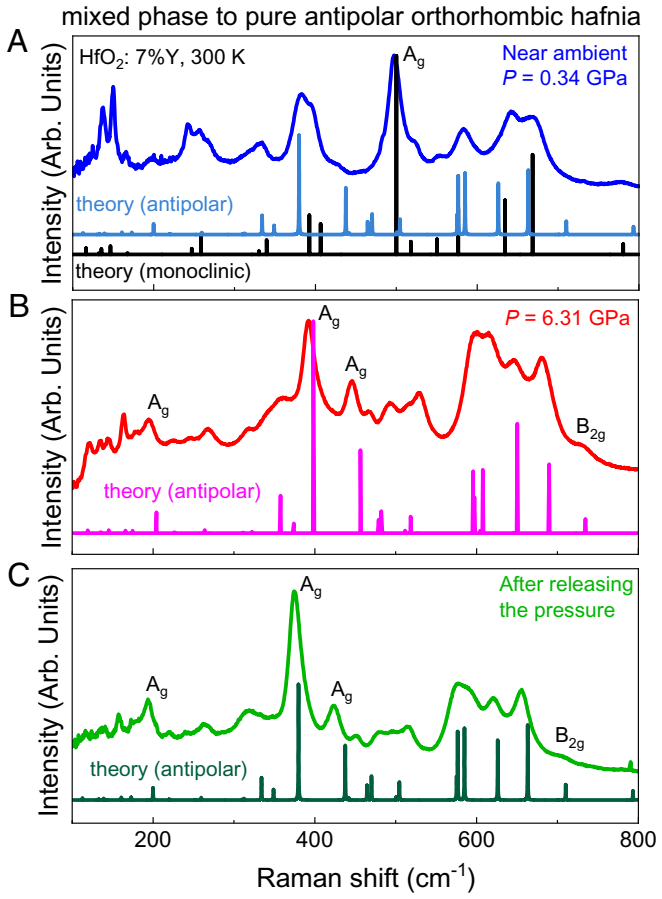

Fig. 2. (*A*) Raman scattering response of HfO_2:7%Y at room temperature in a closed diamond anvil cell. This sample consists of mixed monoclinic + antipolar orthorhombic structures at 0.34 GPa. Theoretically calculated Raman spectra of the pure monoclinic ($P2_1/c$) and antipolar orthorhombic (*Pbca*) phases at zero pressure are plotted below the experimental data. (*B*) Raman scattering response of HfO_2:7%Y at room temperature and $P = 6.3$ GPa. The theoretical Raman spectrum of the antipolar orthorhombic (*Pbca*) phase of hafnia at the same pressure is included below. (*C*) Raman scattering response of HfO_2:7%Y at room temperature after release. As discussed in the main text, a pure antipolar orthorhombic (*Pbca*) phase appears above 6.3 GPa which is trapped upon release of the pressure. The theoretical Raman spectrum at zero pressure is included as well. The symmetries of the signature modes are labeled for each phase (34). Note that there is additional symmetry breaking occurring in the experimental data due to Y stabilizer incorporation (34).

useful for energy storage applications (36). In combination with external stimuli like electric field, the antipolar form of HfO_2 might function as a precursor to the polar phase and, at the same time, provide a platform for unraveling wake-up and fatigue processes (18, 37, 38).

Antipolar Orthorhombic HfO_2:11%Y under Pressure. We also investigated HfO_2:11%Y under compression to examine whether it could be driven into a polar orthorhombic phase with reduced stabilizer concentration. Measurements to 20 GPa did not clearly reveal a transition to the $Pca2_1$ phase (*SI Appendix*, Fig. S3). The system is also fully reversible to the antipolar orthorhombic (*Pbca*) form upon release to ambient pressure conditions. Analysis of the energy landscape, discussed below, demonstrates why this is so.

Pressure-Driven Polar Orthorhombic to Tetragonal Phase Transition in HfO_2:12%Y. In addition to producing clean materials from mixed-phase samples, compression is an external stimulus that can induce structural phase transitions and, via topotactic reaction, create new materials. A key example of such a process is the transformation from polar orthorhombic hafnia to the elusive tetragonal phase in HfO_2:12%Y. We mention the polar orthorhombic to tetragonal transition here to emphasize that compression can also stabilize entirely new phases of hafnia with lower-than-anticipated Y concentrations—at least from the point of view of a laser floating zone + rapid cooling growth protocol (20). Fig. 4 displays the Raman scattering response of HfO_2:12%Y at 0 and 26.74 GPa. The spectra under these conditions clearly correspond well to predictions for the various phonon modes in the polar orthorhombic ($Pca2_1$) and tetragonal ($P4_2/nmc$) phases (34). Even Y-induced defect modes in the high-pressure phase are beautifully predicted and observed. This process is reversible upon release, so the tetragonal phase is not kinetically trapped at room temperature. That said, it may be possible to develop an alternate pathway—perhaps using high-temperature–high pressure routes—to preserve this metastable state. Such an approach differs from using temperature alone to initiate conversion via grain boundary nucleation, which has been shown to yield a polycrystalline tetragonal phase in hafnia nanorods (39).

Enthalpy vs. Pressure Phase Diagram of the Competing Phases of Hafnia. In order to investigate the complex energy landscape and nature of the pressure-induced phase transitions, we performed first-principles density functional theory (DFT) calculations in pure-phase hafnia under pressure. This approach was selected based on our prior work (20), where we demonstrated, by conducting comprehensive DFT calculations on Y:HfO_2

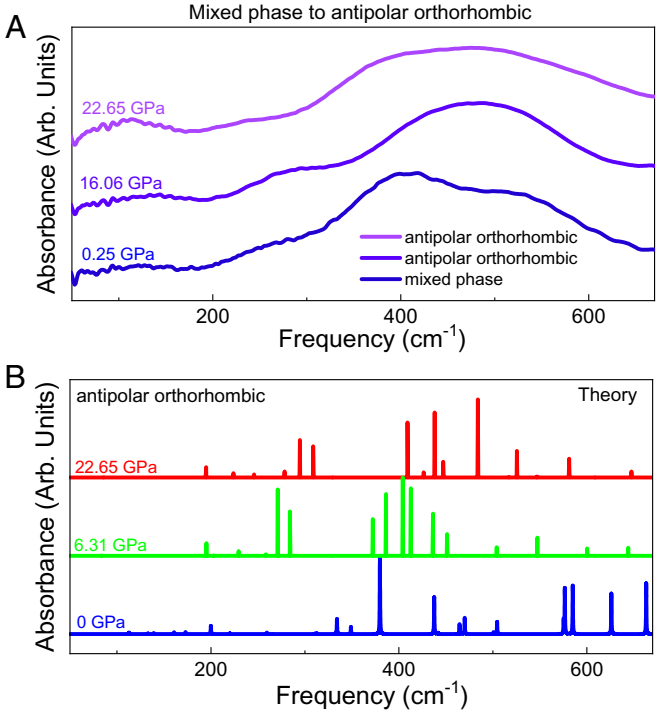

Fig. 3. (*A*) Synchrotron-based infrared absorbance of mixed-phase HfO_2:7%Y as a function of pressure. The antipolar orthorhombic (*Pbca*) phase is formed under compression. Pressures up to 22.65 GPa do not yield the polar orthorhombic phase—at least not in a straightforward manner at room temperature. We also do not see evidence for the cotunnite phases (28), probably due to the presence of Y stabilizer. The spectra are offset for clarity. (*B*) Calculated mode patterns of antipolar orthorhombic (*Pbca*) hafnia at different pressures for comparison.

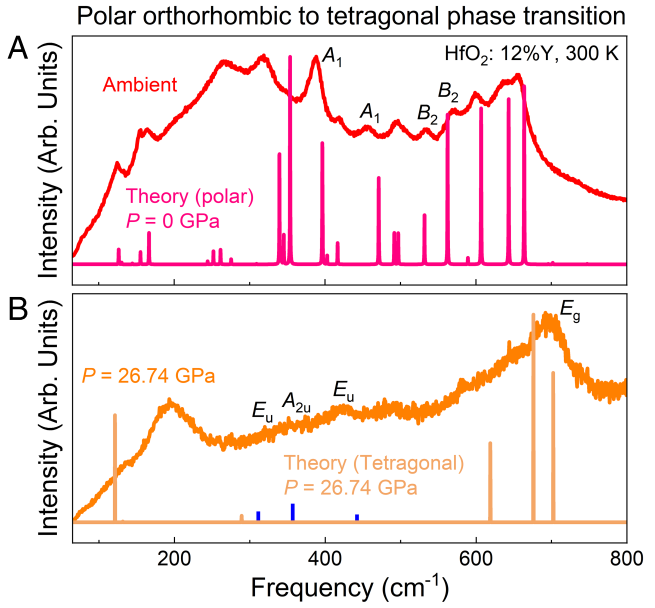

Fig. 4. (*A*) Raman scattering response of HfO_2:12%Y at ambient conditions compared with the results of our lattice dynamics calculations. The symmetries of the signature modes for polar orthorhombic hafnia are labeled. (*B*) Compression drives a transition from the polar orthorhombic ($Pca2_1$) to the tetragonal ($P4_2/nmc$) phase. The theoretically calculated Raman spectrum of tetragonal hafnia is shown for comparison. In addition to the fundamental excitations of the lattice associated with each phase, there is evidence for additional features (shown in blue) that we assign as infrared-active modes appearing due to symmetry breaking induced by Y substitution (34). Based upon the peak shapes, the sample is still in single crystal form at 26.74 GPa.

supercells, that small Y concentrations do not substantially alter the relative formation energy of the various HfO_2 phases. We find that at zero pressure the ground state phase of hafnia is monoclinic (m), followed by orthorhombic antipolar (o-AP), orthorhombic polar (o-P), tetragonal (t), and cubic (c) phases, in the order

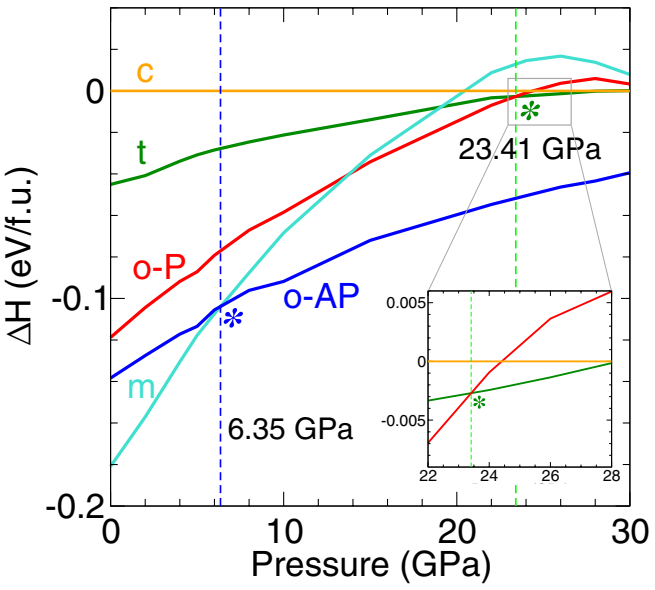

Fig. 5. Enthalpy (ΔH) vs. pressure diagram of the five competing phases of hafnia i.e., cubic (c), tetragonal (t), orthorhombic polar (o-P), orthorhombic antipolar (o-AP), and monoclinic (m), calculated with respect to the cubic phase. Blue and green vertical dashed lines at 6.35 and 23.41 GPa mark the critical pressure where phase transitions are predicted to occur. The *Inset* shows an enlarged view near 23 GPa.

of increasing energy. Our calculated enthalpy vs. pressure phase diagram, shown in Fig. 5, reveals that the orthorhombic antipolar phase becomes the ground state above a critical pressure of 6.35 GPa. This is in remarkable agreement with our experimentally observed phase transition of the mixed monoclinic + orthorhombic antipolar phase sample (HfO_2:7%Y) to the pure orthorhombic antipolar phase at 6.3 GPa (Fig. 2). There is another structural phase transition of interest near 23.4 GPa. Above this critical pressure, the tetragonal phase becomes lower in enthalpy compared to the orthorhombic polar phase implying a possible phase transition from the orthorhombic polar phase to the tetragonal phase. This explains why the orthorhombic polar phase sample (HfO_2:12%Y) transforms into the tetragonal phase above 22 GPa (Fig. 4). Interestingly, tetragonal distortions are predicted to be subtle at pressures above 28 GPa, and tetragonal and cubic phases become almost indistinguishable.

Upon pressure release, HfO_2:12%Y transforms back to the orthorhombic polar phase since it has substantially lower enthalpy compared to the tetragonal phase. On the other hand, HfO_2:7%Y is kinetically trapped in the pure orthorhombic antipolar phase even when pressure is released. This is due to the fact that monoclinic and orthorhombic antipolar phases have competing enthalpies at lower pressures, which makes kinetic trapping possible using our crystal growth technique (i.e., Y substitution and rapid cooling) (20). Under the normal bulk hafnia crystal growth conditions, i.e., no Y substitution and no rapid cooling, the orthorhombic antipolar phase should convert into a monoclinic phase below 6.3 GPa and vice versa (Fig. 5).

Conclusions

Thus far, we measured the vibrational properties of HfO_2:x%Y (x = 7, 11, 12) under compression in order to explore pressure cycling as a route to pure and elusive phases of hafnia. We tested several different pressure pathways as part of this work and found that two types of processes are enabled: developing pure-phase antipolar hafnia from a mixed-phase sample and creating the tetragonal form from the polar orthorhombic material. Pressure cycling is thus a route to high quality as well as more interesting materials. Some of these phases are metastable and do not anneal back to their original state at 300 K. We also point out that pressures like 6 or 20 GPa are minimal compared to 3,300 °C (the temperature for laser floating zone growth of these materials), and high pressure–high-temperature techniques are used routinely in the manufacture of lab-grown diamonds. The ability to employ a room temperature pressure cycle to replace Y stabilizer also has important advantages for flat band preservation, moving us a step closer to realizing the full potential of scale-free ferroelectricity in useful FeRAM devices as well as antiferroelectricity in energy storage applications. Going forward, it will be helpful to explore these effects by X-ray techniques. Our analysis of phase stability in the hafnia system suggests that pressure by itself will not be enough to drive the system into the polar orthorhombic phase. Combined pressure–temperature routes are therefore of future interest. Small strains or nano-sizing may induce similar effects.

Materials and Methods

Crystal Growth and Sample Preparation. High-quality single crystals of hafnia stabilized with yttrium (chemical formula HfO_2:x%Y; x = 0, 7, 11, 12, 20) were grown by laser-diode heated floating zone techniques with rapid cooling as described previously (20). X-ray scattering and TEM images of the materials prepared by this technique are available in ref. 20 as well. This series of materials is summarized in Fig. 1. A small, well-shaped piece of the mixed-

phase material (HfO_2:7%Y) was loaded into a diamond anvil cell equipped with either type IIas or ultra-low fluorescence diamonds. We also studied antipolar orthorhombic HfO_2:11%Y and polar orthorhombic HfO_2:12%Y to a lesser extent. The samples were loaded into diamond anvil cells in the same manner. The diamonds had 400 μm culets, and we employed a pre-indented stainless steel gasket with a 200 μm gasket hole. We used either petroleum jelly or KBr as a pressure medium (depending on the measurement) to assure quasi-hydrostatic pressure conditions. An annealed ruby ball was used to determine pressure via fluorescence (40, 41). We monitor the shape of the ruby fluorescence spectrum to assure that the sample remains in a quasi-hydrostatic environment (*SI Appendix*, Fig. S1). Both the infrared and Raman scattering responses show some orientational dependence that varies from load to load. For the infrared load, the optical density was optimized for significant but non-saturating absorption in order to reveal the features of interest. Annealing tests were carried out in a simple vacuum oven.

Infrared Absorbance and Raman Scattering Measurements. Taking advantage of the stable, high-brightness beam, synchrotron-based infrared spectroscopy (60 to 680 cm^{-1}; 4 cm^{-1} resolution; transmittance geometry) was performed using a Bruker Vertex 80 equipped with a bolometer detector at the 22-IR-1 beamline at the National Synchrotron Light Source II at Brookhaven National Laboratory. Absorbance was calculated as $\alpha(\omega) = -\ln(\mathcal{T}(\omega))$, where $\mathcal{T}(\omega)$ is the measured transmittance. We employed a fast Fourier transform to remove fringes in the data (from the diamond anvil cell and due to the thinness of the sample). Raman scattering was carried out using a single grating system with a 500-mm focal length, a 20× objective with a 30-mm working distance, a 532-nm laser (≤2 mW with a defocused beam), an 1,800-line/mm grating, and a liquid N_2-cooled CCD detector. Spectra were collected for 60 s and averaged 10 times. Pressure was increased between 0 and approximately 25 GPa at room temperature. Sample fluorescence increased significantly at higher pressures, and when that happened, we did not go further. In these cases, infrared spectroscopy was the superior probe. The pressure cycling pathways that we employed are described in the main text. As a reminder, vibrational spectroscopies are incredibly sensitive to symmetry–especially in combination with first principles theory as demonstrated here–providing very specific information on the phases that arise under pressure (34). In any case, we find that the majority of phase transitions are reversible upon release of pressure, although some are irreversible. We discuss these findings in the spirit of highlighting both opportunities and limitations of this pressure cycling technique.

First-Principles Calculations. All the reported DFT calculations were performed using the Vienna Ab initio Simulation Package (VASP) (42–44) within the projector-augmented wave framework (45). The structural parameters for these materials are summarized in *SI Appendix*, Table S1. The generalized-gradient approximation as parameterized by Perdew, Burke, and Ernzerhof (PBEsol) was employed for the exchange-correlation functional (46). The total energy convergence and residual force convergence criteria were set to 10^{-7} eV and 10^{-3} eV/ Å, We used a Monkhorst-Pack *k*-mesh (47) of size $8 \times 8 \times 8$, $12 \times 12 \times 8$, $8 \times 8 \times 8$, $8 \times 8 \times 4$, and $8 \times 8 \times 6$ to sample the reciprocal space of cubic (c), tetragonal (t), orthorhombic polar (o-P), orthorhombic antipolar (o-AP), and monoclinic (m) phases, respectively. Theoretical infrared and Raman spectra were computed using the zone-center phonon eigenvectors and eigen frequencies (34, 48). The Bilbao Crystallographic Server (49) and phonopy package (50) were utilized to determine the Raman selection rules and symmetry of the phonon eigenvectors.

Data, Materials, and Software Availability. All study data are included in the article and/or *SI Appendix*.

ACKNOWLEDGMENTS. J.L.M. acknowledges funding for this work from the Physical Behavior of Materials, Basic Energy Sciences, US Department of Energy (Contract No. DE-SC00023144). S.S. acknowledges support from the University Research Awards at the University of Rochester. SS is also supported by the U.S. Department of Energy, Office of Science, Office of Fusion Energy Sciences, Quantum Information Science program under Award No. DE-SC-0020340. X.X. and S.-W.C. were supported by the center for Quantum Materials Synthesis, funded by the Gordon and Betty Moore Foundation's Emergent Phenomena in Quantum Systems (EPiQS) initiative through GBMF10104 and by Rutgers University. S.S. and K.M.R. appreciate support from the Office of Naval Research grant N00014-21-1-2107. D.V. acknowledges support from NSF grant DMR-1954856. Work at the National Synchrotron Light Source II at Brookhaven National Laboratory is funded by the Department of Energy (DE-AC98-06CH10886). Use of the 22-IR-1 beamline is supported by the National Science Foundation - Earth Sciences via Synchrotron Earth and Environmental Science (SEES) EAR-2223273 and Chicago/DOE Alliance Center (CDAC) DE-NA0003975. We thank Fei-ting Huang for useful discussions.

Author affiliations: [a]Department of Chemistry, University of Tennessee, Knoxville, TN 37996; [b]Department of Physics and Astronomy, University of Tennessee, Knoxville, TN 37996; [c]Department of Mechanical Engineering, University of Rochester, Rochester, NY 14627; [d]Materials Science Program, University of Rochester, Rochester, NY 14627; [e]National Synchrotron Light Source II, Brookhaven National Laboratory, Upton, NY 11973; [f]Department of Physics and Astronomy, Rutgers University, Piscataway, NJ 08854; [g]Rutgers Center for Emergent Materials, Rutgers University, Piscataway, NJ 08854; and [h]Department of Physics, University of Illinois, Chicago, IL 60607-7059

1. U. Schroeder *et al.*, The fundamentals and applications of ferroelectric HfO_2. *Nat. Rev. Mater.* **7**, 653–669 (2022).
2. M.-H. Park *et al.*, Giant negative electrocaloric effects of $Hf_{0.5}Zr_{0.5}O_2$ thin films. *Adv. Mater.* **28**, 7956–7961 (2017).
3. P. Buragohain *et al.*, Nanoscopic studies of domain structure dynamics in ferroelectric La:HfO_2 capacitors. *Appl. Phys. Lett.* **112**, 222901 (2018).
4. Q. Luo *et al.*, A highly CMOS compatible hafnia-based ferroelectric diode. *Nat. Commun.* **11**, 1391 (2020).
5. E. T. Breyer, H. Mulaosmanovic, T. Mikolajick, S. Slesazeck, Perspective on ferroelectric, hafnium oxide based transistors for digital beyond von-Neumann computing. *Appl. Phys. Lett.* **118**, 050501 (2021).
6. C. Liu *et al.*, Robustly stable intermediate memory states in HfO_2-based ferroelectric field-effect transistors. *J. Mater.* **8**, 685–692 (2022).
7. S. Dutta *et al.*, Piezoelectricity in hafnia. *Nat. Commun.* **12**, 7301 (2021).
8. S. S. Cheema *et al.*, Ultrathin ferroic HfO_2-ZrO_2 superlattice gate stack for advanced transistors. *Nature* **604**, 65–71 (2022).
9. Y. Qi *et al.*, Stabilization of competing ferroelectric phases of HfO_2 under epitaxial strain. *Phys. Rev. Lett.* **125**, 257603 (2020).
10. Y. Qi, K. M. Rabe, Phase competition in HfO_2 with applied electric field from first principles. *Phys. Rev. B* **102**, 214108 (2020).
11. F. Delodovici, P. Barone, S. Picozzi, Trilinear-coupling-driven ferroelectricity in HfO_2. *Phys. Rev. Mater.* **5**, 064405 (2021).
12. Y. Qi, S. Singh, K. M. Rabe, Polarization switching mechanism in HfO_2 from first-principles lattice mode analysis. arXiv [Preprint] (2021). https://doi.org/10.48550/arXiv.2108.12538 (Accessed 15 July 2023).
13. T. S. Böscke *et al.*, Ferroelectricity in hafnium oxide thin films. *Appl. Phys. Lett.* **99**, 102903 (2011).
14. C. Li *et al.*, Direct observations of nanofilament evolution in switching processes in HfO_2-based resistive random access memory by in situ TEM studies. *Adv. Mater.* **29**, 1602976 (2017).
15. I. Fina, F. Sánchez, Epitaxial ferrpelectric HfO_2 films: Growth, properties, and devices. *ACS Appl. Elect. Mater.* **3**, 1530–1549 (2021).
16. D.-H. Choe *et al.*, Unexpectedly low barrier of ferroelectric switching in HfO_2 via topological domain walls. *Mater. Today* **50**, 8–15 (2021).
17. H.-J. Lee *et al.*, Scale-free ferroelectricity induced by flat phonon bands in HfO_2. *Science* **369**, 1343–1347 (2020).
18. J. P. B. Silva *et al.*, Progress and perspective on different strategies to achieve wake-up-free ferroelectric hafnia and zirconia-based thin films. *Appl. Mater. Today* **26**, 101394 (2022).
19. B. Cojocaru *et al.*, Phase control in hafnia: New synthesis approach and convergence of average and local structure properties. *ACS Omega* **4**, 8881–8889 (2019).
20. X. Xu *et al.*, Kinetically stabilized ferroelectricity in bulk single-crystalline HfO_2:Y. *Nat. Mater.* **20**, 826–832 (2021).
21. T. Song *et al.*, Impact of La concentration on ferroelectricity of La-doped HfO_2 expitaxial thin films. *ACS Appl. Elect. Mater.* **3**, 4809–4816 (2022).
22. Y. Yun *et al.*, Intrinsic ferroelectricity in Y-doped HfO_2 thin films. *Nat. Mater.* **21**, 903–909 (2022).
23. H. Arashi, Pressure-induced phase transformation of HfO_2. *J. Am. Ceram. Soc.* **75**, 8440847 (1992).
24. A. Jayaraman, S. Y. Wang, S. K. Sharma, L. C. Ming, Pressure-induced phase transformations in HfO_2 to 50 GPa studied by Raman spectroscopy. *Phys. Rev. B* **48**, 9205 (1993).
25. J. M. Leger, A. Atouf, P. E. Tomaszewski, A. S. Pereira, Pressure-induced phase transitions and volume changes in HfO_2 up to 50 GPa. *Phys. Rev. B* **48**, 93 (1993).
26. S. Desgreniers, K. Lagarec, High-density ZrO_2 and HfO_2: Crystalline structures and equations of state. *Phys. Rev. B* **59**, 8467 (1999).

27. J. Kang, E.-C. Lee, K. J. Chang, First-principles study of the structural phase transformation of hafnia under pressure. *Phys. Rev. B* **68**, 054106 (2003).
28. O. Ohtaka *et al*., Phase relations and volume changes of hafnia under high pressure and high temperature. *J. Am. Ceram. Soc.* **84**, 1369–1373 (2004).
29. Y. Al-Khatatbeh, K. K. M. Lee, B. Kiefer, Phase diagram up to 105 GPa and mechanical strength of HfO_2. *Phys. Rev. B* **82**, 144106 (2010).
30. T. D. Huan, V. Sharma, G. A. Rossetti, R. Ramprasad, Pathways towards ferroelectricity in hafnia. *Phys. Rev. B* **90**, 064111 (2014).
31. G. Mandal, R. Jana, P. Saha, P. Das, Study of structural phase transition of HfO_2 at high pressure. *Mater. Today: Proc.* **3**, 2997–3001 (2016).
32. T. Cao *et al*., Stabilizing polar phases in binary metal oxides by hole doping. *Phys. Rev. Mater.* **7**, 044412 (2023).
33. T. Mikolajick, U. Schroeder, Ferroelectricity in bulk hafnia. *Nat. Mater.* **20**, 718–719 (2021).
34. S. Fan *et al*., Vibrational fingerprints of ferroelectric HfO_2. *npj Quant. Mater.* **7**, 32 (2022).
35. U. Schroeder *et al*., Using Raman spectroscopy and X-ray diffraction for phase determination in ferroelectric mixed $Hf_{1-x}Zr_xO_2$-based layers. *J. Appl. Phys.* **132**, 21 (2022).
36. Z. Liu *et al*., Antiferroelectrics for energy storage applications: A review. *Adv. Mater. Tech.* **3**, 1800111 (2018).
37. P. Jiang *et al*., Wake-up effect in HfO_2-based ferroelectric films. *Adv. Elect. Mater.* **7**, 2000728 (2021).
38. Y. Cheng *et al*., Reversible transition between the polar and antipolar phases and its implications for wake-up and fatigue in HfO_2-based ferroelectric thin films. *Nat. Commun.* **13**, 645 (2022).
39. B. M. Hudak *et al*., Real-time atomistic observation of structural phase transformations in individual hafnia nanorods. *Nat. Commun.* **8**, 15316 (2017).
40. H. K. Mao, P. M. Bell, J. W. Shaner, D. J. Steinberg, Specific volume measurements of Cu, Mo, Pd, and Ag and calibration of the ruby R_1 fluorescence pressure gauge from 0.06 to 1 Mbar. *J. Appl. Phys.* **49**, 3276–3283 (1976).
41. H. K. Mao, J. Xu, P. M. Bell, Calibration of the ruby pressure gauge to 800 kbar under quasi-hydrostatic conditions. *J. Geophys. Res.* **91**, 4673–4676 (1986).
42. G. Kresse, J. Furthmüller, Efficient iterative schemes for *ab initio* total-energy calculations using a plane-wave basis set. *Phys. Rev. B* **54**, 11169–11186 (1996).
43. G. Kresse, J. Furthmüller, Efficiency of *ab-initio* total energy calculations for metals and semiconductors using a plane-wave basis set. *Comput. Mater. Sci.* **6**, 15–50 (1996).
44. G. Kresse, D. Joubert, From ultrasoft pseudopotentials to the projector augmented-wave method. *Phys. Rev. B* **59**, 1758–1775 (1999).
45. P. E. Blöchl, Projector augmented-wave method. *Phys. Rev. B* **50**, 17953–17979 (1994).
46. J. P. Perdew *et al*., Restoring the density-gradient expansion for exchange in solids and surfaces. *Phys. Rev. Lett.* **100**, 136406 (2008).
47. H. J. Monkhorst, J. D. Pack, Special points for Brillouin-zone integrations. *Phys. Rev. B* **13**, 5188–5192 (1976).
48. J. M. Skelton *et al*., Lattice dynamics of the tin sulphides SnS_2, SnS and Sn_2S_3: Vibrational spectra and thermal transport. *Phys. Chem. Chem. Phys.* **19**, 12452–12465 (2017).
49. E. Kroumova *et al*., Bilbao crystallographic server: Useful databases and tools for phase-transition studies. *Phase Transit.* **76**, 155–170 (2003).
50. A. Togo, I. Tanaka, First principles phonon calculations in materials science. *Scr. Mater.* **108**, 1–5 (2015).